Influence of anodization time on the surface modifications on α-Fe₂O₃ photoanode upon anodization

Kelebogile Maabong[a)]
Department of Physics, University of Pretoria, Pretoria 0028, South Africa; Laboratory of High Ceramics, Empa, Swiss Federal Laboratories for Materials Science and Technology, CH-8600 Dübendorf, Switzerland; and Department of Physics, University of Botswana, UB 0022 Gaborone, Botswana

Yelin Hu
Laboratory of High Ceramics, Empa, Swiss Federal Laboratories for Materials Science and Technology, CH-8600 Dübendorf, Switzerland; and Laboratory for Photonics and Interfaces, EPFL, Ecole Polytechnique Federale de Lausanne, CH-1015 Lausanne, Switzerland

Artur Braun
Laboratory of High Ceramics, Empa, Swiss Federal Laboratories for Materials Science and Technology, CH-8600 Dübendorf, Switzerland

Augusto G.J. Machatine
Department of Physics, University of Pretoria, Pretoria 0028, South Africa

Mmantsae Diale[b)]
Department of Physics, University of Pretoria, Pretoria 0028, South Africa; and Laboratory of High Ceramics, Empa, Swiss Federal Laboratories for Materials Science and Technology, CH-8600 Dübendorf, Switzerland

In searching for a suitable semiconductor material for hydrogen production via photoelectrochemical water splitting, α-Fe₂O₃ received significant attention as a promising photoanode due to its band gap (~2.1 eV), good stability, low cost, and natural occurrence. α-Fe₂O₃ thin films were prepared by economic and facile dip coating method and subsequently subjected to an anodic potential of 700 mV versus Ag/AgCl in 1M KOH for different anodization times (1, 10, and 900 min) under illumination. X-ray diffractometry revealed increase in crystallites size from ~31 nm for nanoparticles in pristine state to ~38 and 44 nm after anodization for 1 and 900 min, respectively. A clear positive correlation between anodization time and grain (particle) size was observed from field emission gun scanning electron microscopy and atomic force microscopy (AFM); longer exposure time to anodizing conditions resulted in larger grains. Grain size increased from ~57.9 nm in pristine state to ~153.5 nm after anodization for 900 min. A significant smoothening of the surface with increase in anodization time was evident from AFM analysis.

1. Introduction

Direct solar hydrogen production through photoelectrochemical (PEC) water splitting presents an enticing route to supply the world's increasing energy demand with a renewable chemical fuel.[1–5] Fuel production from photoelectrolysis of water at semiconductor electrode was first reported in 1972 using TiO₂ (anatase) photoanode.[6] Due to its large band gap, TiO₂ yielded low efficiencies. However, the idea intrigued investigations on identifying an ideal and affordable photoactive semiconductor material with good absorptive capacity in the entire visible region of the solar spectrum and outstanding charge transfer properties. Hematite (α-Fe₂O₃) received a great-deal of attention as a promising photoanode material.[2–4,7–11] A band gap of ~2.0 eV, low cost, good stability against dissolution in aqueous electrolyte, and nontoxicity make it attractive for water splitting. However, despite the good characteristics, α-Fe₂O₃ is still not yet an effective photoanode for water to solar fuel application,[4] due to poor charge transport properties and high rate of carrier recombination.[5] Furthermore, the nonoptimal alignment of its conduction band and H₂ evolution potential for water reduction presents another challenge for practical implementation of α-Fe₂O₃ photoanode.[4] Consequently, a bias of over 1 V versus the reversible hydrogen electrode is required to drive splitting reactions.[4,12] Upon contact with the electrolyte in a biased cell, electrochemical reactions take place even at room temperature, such as electrochemical corrosion, electrochemical reduction, or oxidation of species in

solution, and even catalysis, which all depend fundamentally on steps involving electron transfer.[13] Electrode reactions (oxidation and reduction) may lead to the formation of an oxide layer on the anode surface.[4]

Anodization is an electrochemical process which could create a thick compact oxide layer of metal surfaces that may increase resistance to corrosion of the surface.[14] The growth of the oxide film involves the transport of matter and charge between different phases, like metal, oxide and anodizing medium. Bora et al.,[15] point to electrochemical oxidation (anodization) as an operational step in functionality of biased PEC cells. During anodization the applied anodizing potential causes ionization of F^{2+} to Fe^{3+} cations [$Fe^{2+} \rightarrow Fe^{3+} + e^-$] as well as dissociation of water and possibly the electrolyte to occur at the oxide-electrolyte interface.[16] Moreover, a significant amount of anions is supplied by water dissociation due to water splitting process. Some of the metal ions combine with oxygen anions and form metal oxide at the oxide-electrolyte interface.[16,17] Apparently, a thin layer of oxide film grows by both outward and inward diffusion of ions through the oxide-electrolyte interface and simultaneously oxidation heat is generated.[13,18] The formation process of this anodic oxide is a complex process involving physics, chemistry and electrochemistry. Both chemical dissolution and electric field dissolution play role in the structure and composition of the formed anodic film, particularly at the oxide-electrolyte surface.[18] The thickness of the formed oxide layer is influenced by the charge passed (i.e., product of current density and time) whereas, the morphology and composition depend on the anodizing conditions such as anodizing potential and time, reaction temperature, and electrolyte type, pH and concentration.[19,20] The surface undergoes extensive morphological reorganization upon anodization. The oxide scales are in continuous transformation including grain growth, phase transformation, porosity, precipitation, recrystallization, development, and thickening that depend on anodizing conditions.[21] All these parameters may influence the photoresponse of the photoanode.

Although a significant improvement has been made on conductivity of α-Fe_2O_3 by elemental doping[5,22–25] and nanostructuring,[26–29] the influence of the anodizing process on the photocatalytic performance of α-Fe_2O_3 photoanode in a PEC cell has not been extensively studied. However, a detailed research on the surface molecular structure of anodized α-Fe_2O_3 photoanode has been conducted and reported transformation of Fe^{2+} to Fe^{3+} states at the surface upon subject to anodizing conditions and the findings were attributed to filling of oxygen vacancies due to increasing oxygen content at the surface.[9,15,30,31] Recently, x-ray diffractometry revealed significant modifications on the crystallographic structure and morphology at the surface upon anodization at 500 mV versus Ag/AgCl for just 1 min.[32] In particular,

a significant grain growth at the surface by a 3 factor of magnitude was observed. Microstructure, in particular the crystallinity, crystallite size, shape, spatial distribution, and morphology have an important influence on electrical, optical, and catalytic properties of semiconductor materials.[33] Therefore, a complete understanding of the influence of anodization process on the microstructure of α-Fe_2O_3 photoanode is vital in improving the PEC performance of α-Fe_2O_3 photoelectrode. This study aimed toward investigating the influence of anodization (exposure) time on the surface modifications on α-Fe_2O_3 photoanode caused upon anodization in PEC cell. For this, we carried out structural and morphological analysis of α-Fe_2O_3 photoanode electrochemically oxidized at an applied anodic potential of 700 mV versus Ag/AgCl in 1 M KOH under illumination, for different exposure times. To the best of our knowledge, no similar results have been reported.

2. Experimental Section

A. Electrode preparation

α-Fe_2O_3 thin films were synthesized by dip coating of a precursor complex on a conductive fluorine-doped tin oxide (FTO) coated glass substrate in a systematic procedure described in Fig. 1. The FTO Substrates were cleaned in an ultrasonic bath of acetone and isopropanol for 30 min, rinsed with ethanol and dry blown with compressed N_2 (99.95%). The precursor complex was synthesized by heating a mixture of iron (III) nitrate ($Fe(NO_3)_3 \cdot 9H_2O$) and oleic acid ($C_{18}H_{34}O_2$) to 125 °C while continuously stirring to give a red-brown viscous mass which was then cooled to room temperature, left for 24 h to dry, and subsequently treated with 80 mL of tetrahydrofuran. The resultant supernatant solution was stirred with a glass rod to dissolve the contents and the powdery precipitate was separated from the solution by centrifugation (4000 rpm) for 15 min. The precursor complex
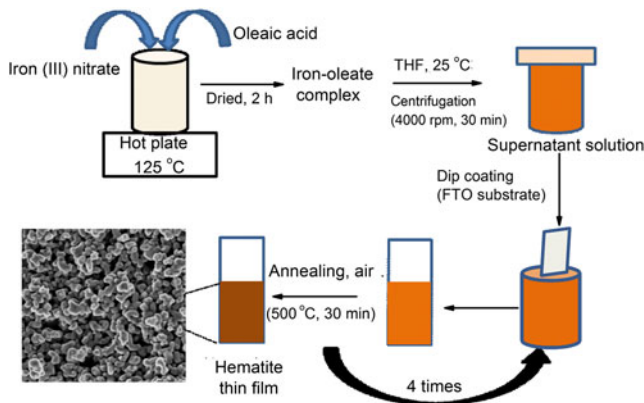

Fig. 1. A schematic diagram of the systematic procedure for preparation of pristine α-Fe_2O_3 photoanode nanoparticles.

2

was recovered for the dip coating of the film. α-Fe$_2$O$_3$ thin films of 4 layers of average thickness of 530 nm were obtained by repeated dip coating and annealing at 500 °C for 30 min for each layer.

B. Electrochemical oxidation process

The electrochemical oxidation (anodization) was carried out in a three-electrode PEC cell (also known as a "cappuccino cell", manufactured from PEEK plastic, Radiometer Analytical, Lyon, France),[31] as shown in Fig. 2. α-Fe$_2$O$_3$/FTO, a platinum plate (0.5 cm $\times$ 0.5 cm), and Ag/AgCl in saturated KCl were used as the working (anode), cathode, and reference electrode, respectively. A potentiostat (*Voltalab80 PGZ 402*, Radiometer Analytical) interfaced with a PC was used in all the measurements. The anodic potential of 700 mV was applied for 1, 10, and 900 minutes in 10 cm^3 of 1 M KOH (pH = 13.8) under 1.5 AM simulated light conditions with a UV-filtered xenon lamp. The anodized samples were washed with distilled water to remove the occluded ions from the anodized solutions and left to dry in air.

C. Characterization of the samples

The phase purity of the films was confirmed by the powder x-ray diffraction (XRD) (PANanalytical X'Pert PRO, Almelo, The Netherlands) with Co K$_{\alpha\text{-}1}$ radiation (λ = 0.178901 nm). The surface morphology analysis of the films was investigated with a field emission gun scanning electron microscopy (FEG-SEM) employing Zeizz Ultra
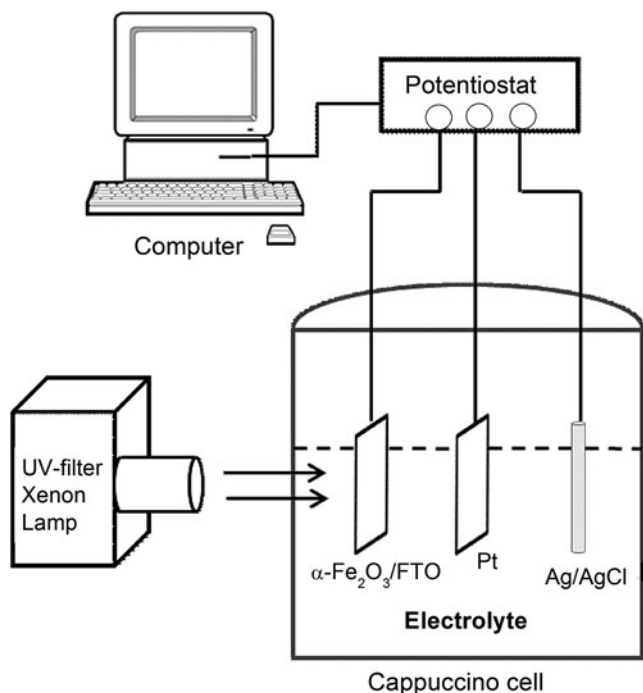

Fig. 2. A schematic diagram of the anodizing apparatus, three-electrode PEC cell.

55 instrument (Carl Zeiss AG, Goettingen, Germany) fitted with the usual SEM detectors and in-lens detector. The surface topography of the films was examined using the Nanoscope atomic force microscopy (AFM) operating in the tapping mode at a scan rate of 0.4 Hz. The average thickness was obtained by a surface profiler.

3. Results and Discussion

Figure 3 shows the XRD pattern for the as-prepared films (pristine) and after the films were anodized for 1, 10, and 900 min under illumination. The (104) and (110) peaks were observed in all the films which confirmed the α-phase formation of rhombohedral iron oxide with $R\bar{3}c$ space group. Other reflections corresponding to (012), (006), (113), (202), (024), (116), and (018) planes were also observed in all the films. No diffraction peaks of any other impurities of iron oxide phases were detected, indicating high purity of the synthesized α-Fe$_2$O$_3$ thin films.

The peaks were generally sharp and narrow with small full width at half maximum (FWHM) indicating high crystallinity of the samples. The expanded XRD pattern
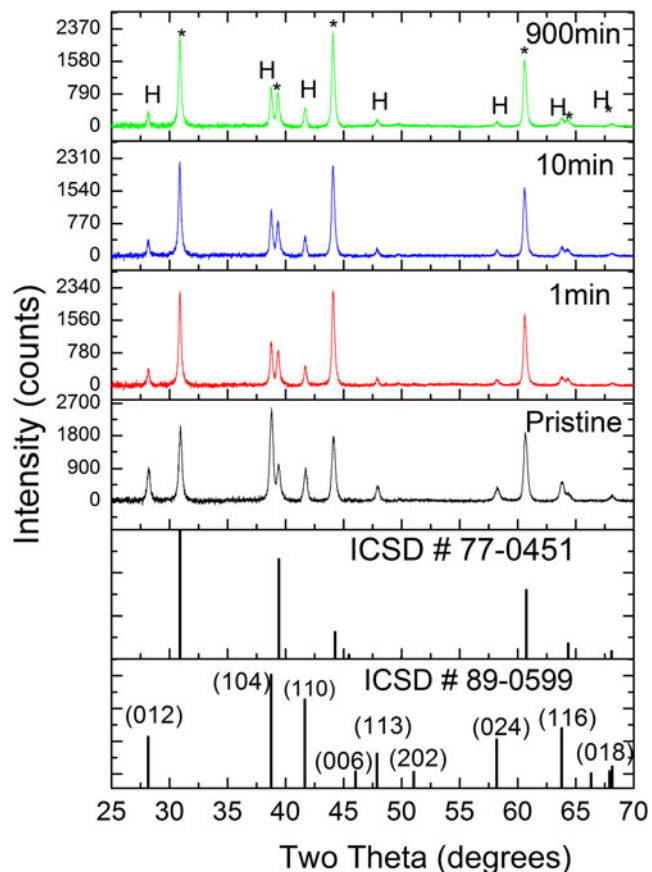

Fig. 3. XRDs of dip coated pristine and anodized α-Fe$_2$O$_3$ films (marked with H) deposited on F:SnO$_2$ substrates. The peaks marked with (*) corresponds to SnO$_2$ originating from the substrate. The standard powder pattern of α-Fe$_2$O$_3$ [ICSD #89-0599] and SnO$_2$ [ICSD #77-0451] are also included.

of the films in Fig. 4(a) shows decreasing peaks intensity and linewidths upon anodization. A close inspection and comparison of the (104) peaks in Fig. 4(b) clearly demonstrate decreasing linewidths at half maximum with increasing anodization time, suggesting increase in crystallites size of the anodized nanoparticles. A pronounced effect on the peaks width and intensity between the pristine and anodized films was observed. No noticeable difference between the anodized films was observed regardless of the anodization times.

The extracted FWHM values for the prominent reflections (012), (104), and (110) and the corresponding average crystallite size, D, as extracted from the peak width analysis and estimated according to Debye–Scherrer formula[34] are presented in Table I. The estimated average crystallite size was observed to range from $\sim$31 to 44 nm. The obtained crystallite size range values are close to values previously obtained for the films that were subjected to 500 mV constant anodic potential for 1 min,[32] regardless of the difference in exposure time. There was no clear correlation between crystallite size and anodization time.

The dislocation density δ, which represents the amount of defects or imperfections in the film, is given as $\delta = 1/D^2$.[35] The calculated values of δ for all the films are also given in Table I. The smaller FWHM and larger D values indicate better crystallization of the film. Dislocation densities exhibit a decreasing trend with increasing anodization time, which implies decrease in the concentration of lattice imperfections.

The role of exposure time on grain growth in anodized α-Fe$_2$O$_3$ photoanode is clearly illustrated by FEG-SEM top-view micrographs of the prepared films in Fig. 5, taken prior to and after anodization. The method of preparation is considered an important factor that significantly affects the surface properties of the nanoparticles. During annealing, excess hematite was peeled off from the surface and excess film was removed before the next dipping step. However, surface analysis by SEM still revealed peeling off (not shown) of the top layer which

consisted of typical dumbbell shaped nanoparticles, shown in Fig. 5(a) for pristine and (b and c) anodized films for 1 and 900 min, respectively. The exposed sublayer underneath showed spherical nanoparticles [Figs. 5(d)–5(g)]; (d)-pristine and (e and g)-anodized films. On both parts of the films (top and exposed sublayer), increase in grain size was demonstrated. Prior to anodization, the films exhibit small sized-grains which recrystallized, grew and reorganized upon anodization. The nonanodized top layer showed less porous surface with an average grain size of $\sim$42.9 nm. Upon anodiza-tion, the layer became more porous with average grain size increasing to $\sim$62.3 and 99.4 nm after being subjected to anodic conditions for 1 and 900 min, respectively. During anodic anodization, the oxidation heat produced leads to dissolution of the oxide by the electrolyte particularly at oxide-electrolyte interface, resulting in porous oxide layer.[18] The spherical grains on the exposed layer increased from approximately 57.9 nm in pristine state to 153.5 nm for films anodized for 900 min.

As the anodization process continues, both the cation and anion ions migrate between the bulk oxide and the electrolyte through the film pores and the film gets thicker and denser. Probably, a thin layer of oxide is formed thorough diffusion of metal cations and oxygen anions. The relatively thin, nonporous oxide layer under the

Table I. A presentation of the FWHM, average crystallites size (D) and dislocation density (δ) of the α-Fe$_2$O$_3$ nanoparticles before and after electrochemical oxidation in 1M KOH at 700 mV at different anodization times.

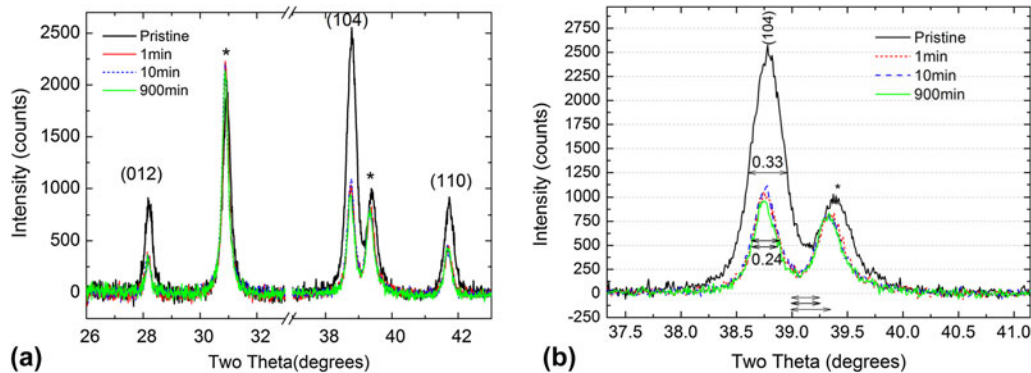| Anodization time (min) | FWHM (2θ) | | | D (nm) | |
	(012)	(104)	(110)	XRD	δ (10^{18} m^{-2})
0	0.324	0.331	0.34	31	0.00100
1	0.261	0.271	0.28	38	0.00069
10	0.247	0.26	0.27	39	0.00066
900	0.224	0.24	0.24	44	0.00052

Fig. 4. Expanded XRD pattern of the prominent Bragg reflections of α-Fe$_2$O$_3$ films (a) and close inspection of (104) peak (b) showing decreasing peak linewidth (FWHM) upon anodization.
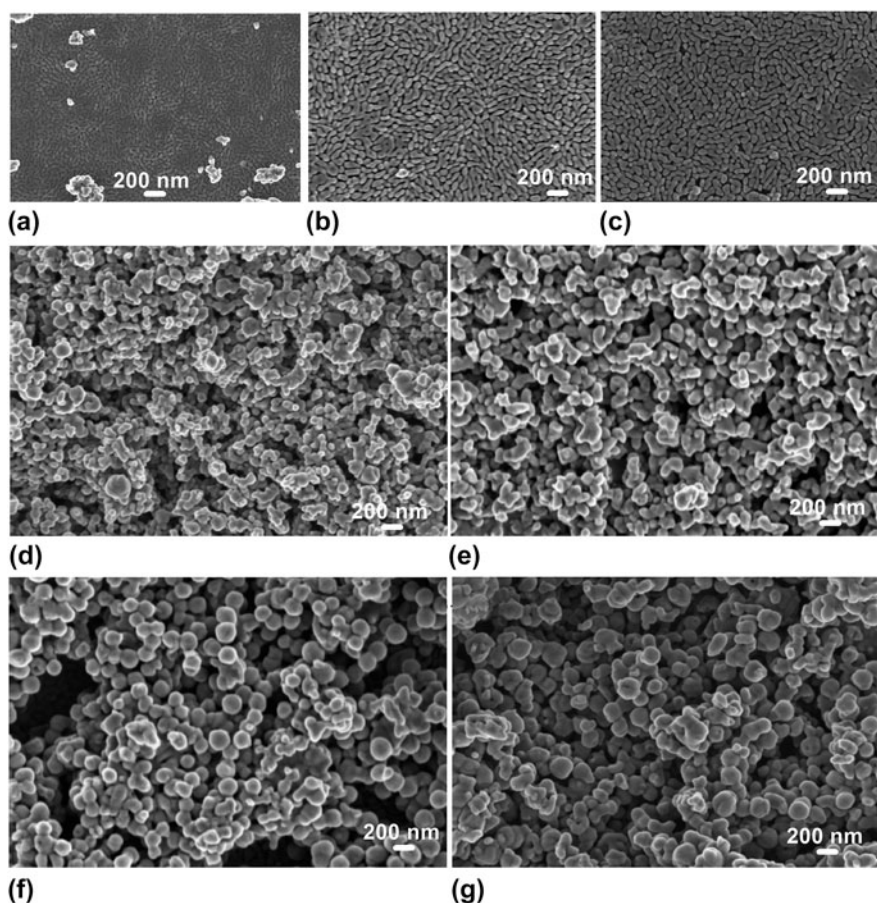
Fig. 5. FEG-SEM top-view images of α-Fe₂O₃ films before and after anodization at 700 mV in 1M KOH, measured from top layer [(a) before,(b) 1, (c) 900 min] and exposed sublayer [(d) before, (e) 1, (f) 10, (g) 900 min].

porous oxide structures is considered to contribute to the improvement of corrosion resistance of the oxide.[36] It should be noted that because of the nature of the preparation method used in this study, the films were rough and the difference in film thickness could not be detected using a surface profiler. In contrast to crystallites size, the effect of anodization time on grain size is more significant. The grain size observed from FEG-SEM images is larger than the crystallite size from XRD analysis. The grains increased in size probably by coalescence of neighboring grains during reorganization of the surface and form large grain.[17]

The 3D top-view AFM images in Fig. 6 (measured form the exposed layer) clearly confirmed FEG-SEM analysis. The size of the grains on the surface increased with anodization time. Prior to anodization, the grains were not visible on the surface, due to loosely attached α-Fe₂O₃ grains.[37] The poor-adherence was confirmed by the maximum height of the film. Upon being subjected to anodization conditions for only 1 min, a significant change on the surface topography was observed with nanoparticles becoming clearly visible on the surface. The anodized sample images show increasing grain size

with increasing anodization time. Like FEG-SEM, the average grain size increased from approximately ~58.4 nm for nanoparticles in pristine state to approximately 88–149.5 nm for films anodized for 1 min (shortest time) and 900 min (longest time), respectively. The grain size values are in agreement with the FEG-SEM analysis as shown in Table II. Long anodization time resulted in larger nanocrystals.

The surface roughness of all the samples was extracted from AFM images and presented against anodization time in Fig. 7. Generally, the films were rough. The pristine films surface exhibits a larger root-mean-square (rms) roughness of ~49.4 nm. However, a rapid decrease in the rms roughness was observed upon anodization for 1 min. The rms value decreased with increasing anodization time as the particles became larger. The decrease in rms value may be ascribed to dissolution of rough spots upon anodization. Surface roughness plays an important role in various processes, such as adhesion and light scattering, and can significantly affect the PEC performance of the α-Fe₂O₃ nanostructures.

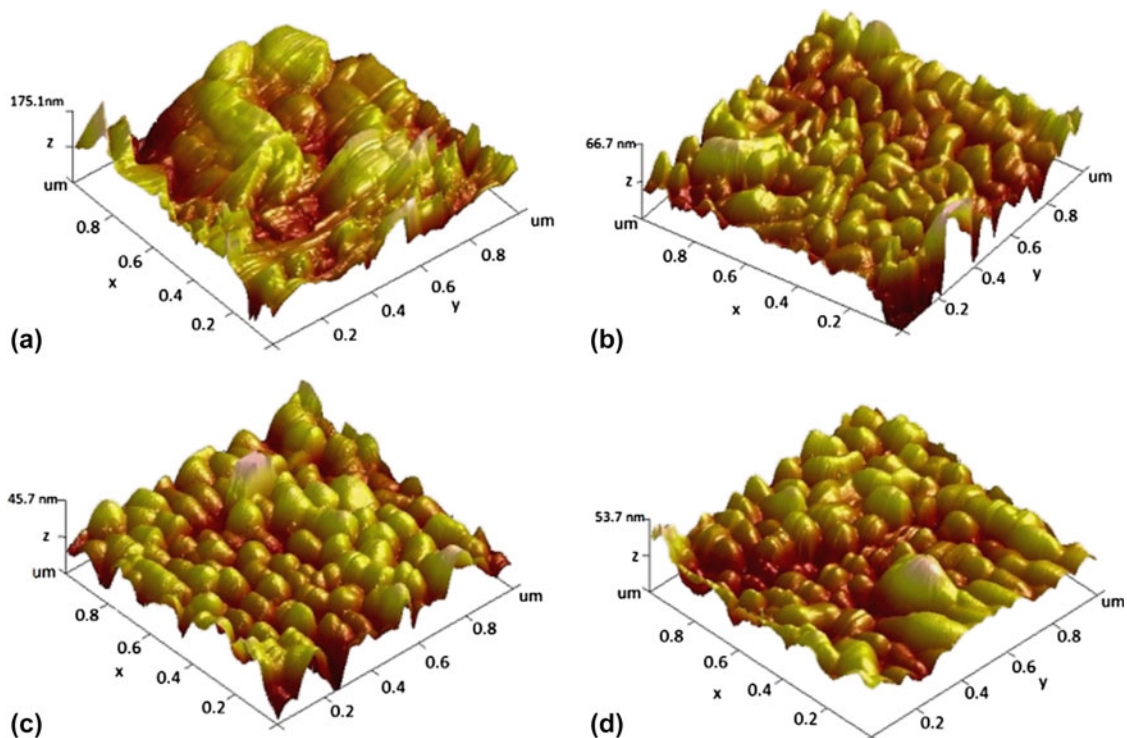The scattering and absorption coefficients of α-Fe₂O₃ depend on particle size, shape, density, surface roughness

5

Fig. 6. 3D AFM images of α-Fe$_2$O$_3$ nanoparticles before (a) and after anodization at 700 mV in 1 M KOH for 1 min (b), 10 min (c) and 900 min (d).

Table II. A comparison of surface roughness of the hematite nanoparticles before and after electrochemical oxidation in 1M KOH at 700 mV at different anodization times.

Anodization time (min)	Particle size (nm)		Surface roughness (nm)
	FESEM	AFM	
0	57.9	58.4	49.4
1	88.3	88.0	17.9
10	121.8	117.3	12.7
900	153.5	149.5	15.4

and spatial arrangement of the particles, morphology, and refractive index. Small particles of hematite are less absorbing than large particles.[38] Thus, enhancement in UV-vis optical absorbance observed in anodized films (Fig. 8) may be attributed to increased grain size and thickness of the oxide. The onset absorbance wave length occurred at 592 nm for pristine nanoparticles, and 598 and 596 for films anodized for 1 min and 900 min, respectively. A shift to higher wave length in anodized films may be attributed smoothening of the surface and grain growth upon anodization.

4. Discussion

The film formation and grain growth mechanism upon anodization of a pre-existing oxide film is a complex process although one may establish a number of
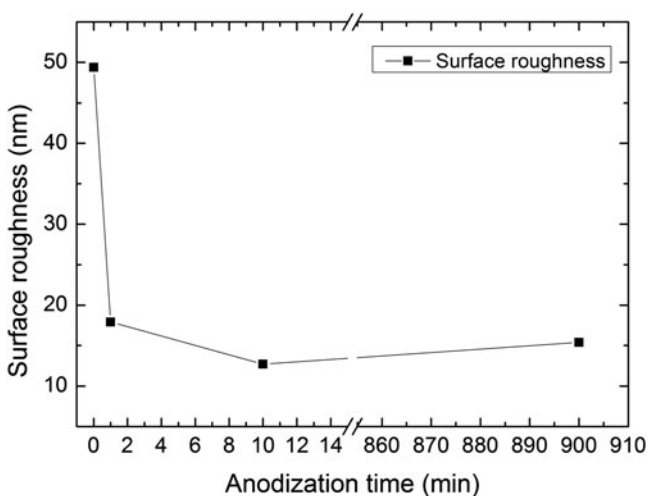

Fig. 7. Surface roughness of α-Fe$_2$O$_3$ films versus anodization time.

analogies with anodization of metal surfaces. Previous studies discussed different factors as possible source of heat during anodization, for example (i) oxidation reaction heat and convectional joule heating (electrical power dissipated) of the electrolyte,[18] (ii) burning of the oxide under illumination.[13] Excitation of nanoparticles with UV-visible light leads to generation of a large number of carriers. Majority of these carriers recombine nonradiatively before contributing to water splitting. Thus, the energy released from nonradiative
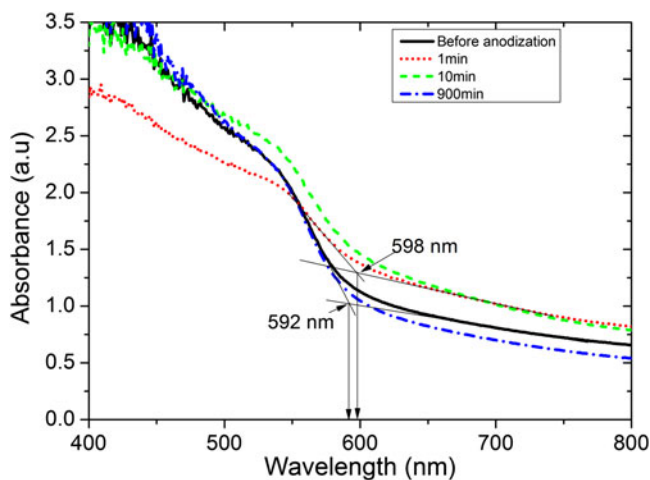
6

Fig. 8. UV-vis absorption spectra of the α-Fe₂O₃ prior to and after anodization.

recombination heats up the oxide surface. Probably grain growth occurs likely due to Ostwald ripening; whereby large particles grow at the expense of small particles as a result of increase in temperature at the surface. Smaller grains which have a higher solubility than larger ones slowly dissolve and redeposit on the large crystals and simultaneously grain growth occurs. According to Heiroth et al.,[33] grain growth process in polycrystalline material is driven by the minimization of the total grain boundary per area. During recrystallization and growth processes, the number of grain boundaries decreases due to the annihilation of small grains by grain boundary migration.[39] The smaller primary particles have large surface free energy and tend to agglomerate, coalesce, and grow into larger grains.[17,40] The rotation-coalescence of neighboring grains results in elimination of grain boundaries between them and supposedly grain growth. Therefore, grain growth upon anodization is expected to reduce recombination rate of holes and electrons and subsequently enhance conductivity of the photoelectrode.[41] Photoconductivity measurements of the anodized films were not done in this study. However, Braun et al.,[31] reported enhanced current density on anodized hematite after the films were subjected to anodic potential of 200 and 600 mV in 1M KOH for 24 h. The enhancement on conductivity may be attributed to improved surface upon anodization. Gajda-Schrantz et al.,[30] reported on study of molecular structure of the anodized films by XPS analysis, which suggested reduction of surface states (Fe^{2+}) on the surface upon anodization. Although, the presence of Fe^{2+} on the surface appears essential, these states have a considerable influence on the kinetics of the electron processes occurring at the semiconductor–liquid junction, acting as additional recombination centers, interband trapping levels and intermediate centers that may shorten the lifetime of photogenerated carriers and yield low photocurrent.[42]

5. Conclusion

The influence of exposure time on the surface crystallographic structure modifications on hematite (α-Fe₂O₃) photoanode upon anodization in PEC cell was investigated. α-Fe₂O₃ thin films prepared by economic and facile dip coating method were anodized in 1M KOH at an anodic potential of 700 mV versus Ag/AgCl under simulated illumination. The crystallite size increased from ~31 nm for nanoparticles in pristine state to ~38 and 44 nm after anodization for 1 min (shortest time) and 900 min (longest time), respectively, without losing the crystallinity. A positive clear correlation between anodization time and grain size was observed from FEG-SEM and AFM. Grain size increased with increasing anodization time from ~57.9 nm in pristine state to ~153.7 nm for films exposed for 900 min; longer exposure time to anodizing conditions resulted in larger grains. This increase in grain size during anodization is expected to improve conductivity of α-Fe₂O₃ due to reduced recombination rate of holes and electrons as a result of improvement on the surface of the electrode during anodization. Density of dislocations, surface roughness, and possibly grain boundaries decreased.

Acknowledgment

References

1. B. Klahr, S. Gimenez, F. Fabregat-Santiago, J. Bisquert, and T.W. Hamann: Electrochemical and photoelectrochemical investigation of water oxidation with hematite electrodes. *Energy Environ. Sci.* **5**(6), 7626 (2012).

2. M. Grätzel: Photoelectrochemical cells. *Nature* **414**(15), 338 (2001).

3. K. Sivula, F. Le Formal, and M. Gratzel: Solar water splitting: Progress using hematite (alpha-Fe₂O₃) photoelectrodes. *ChemSusChem* **4**(4), 432 (2011).

4. M.J. Katz, S.C. Riha, N.C. Jeong, A.B.F. Martinson, O.K. Farha, and J.T. Hupp: Toward solar fuels: Water splitting with sunlight and "rust"? *Coord. Chem. Rev.* **256**(21–22), 2521 (2012).

5. I. Cesar, K. Sivula, A. Kay, R. Zboril, and M. Grätzel: Influence of feature size film thickness and silicon doping on the perfomance of nanostructured hematite photoanodes for solar water splitting. *J. Phys. Chem. C* **113**, 772 (2009).

6. A. Fujishima and K. Honda: Electrochemical photolysis of water at a semiconductor electrode. *Nature* **238**(5358), 37 (1972).

7. A. Duret and M. Grätzel: Visible light-induced water oxidation on mesoscopic α-Fe₂O₃ films made by ultrasonic spray pyrolysis. *J. Phys. Chem. B* **109**(36), 17184 (2005).

8. D.K. Bora, A. Braun, and E.C. Constable: "In rust we trust". Hematite—The prospective inorganic backbone for artificial photosynthesis. *Energy Environ. Sci.* **6**(2), 407 (2013).

9. A. Braun, K. Sivula, D.K. Bora, J. Zhu, L. Zhang, M. Grätzel, J. Guo, and E.C. Constable: Direct observation of two electron holes in a hematite photoanode during photoelectrochemical water splitting. *J. Phys. Chem. B* **116**(32), 16870 (2012).

10. H. Dotan, K. Sivula, M. Grätzel, A. Rothschild, and S.C. Warren: Probing the photoelectrochemical properties of hematite (α-Fe$_2$O$_3$) electrodes using hydrogen peroxide as a hole scavenger. *Energy Environ. Sci.* **4**(3), 958 (2011).

11. F. Boudoire, R. Toth, J. Heier, A. Braun, and E.C. Constable: Hematite nanostructuring using electrohydrodynamic lithography. *Appl. Surf. Sci.* **305**, 62 (2014).

12. F. Le Formal, N. Tétreault, M. Cornuz, T. Moehl, M. Grätzel, and K. Sivula: Passivating surface states on water splitting hematite photoanodes with alumina overlayers. *Chem. Sci.* **2**(4), 737 (2011).

13. S.R. Morrisons: *The Chemical Physics of Surface* (Plenum Press, New York, 1977).

14. R.R. Rangaraju, A. Panday, K.S. Raja, and M. Misra: Nano-structured anodic iron oxide film as photoanode for water oxidation. *J. Phys. D: Appl. Phys.* **42**(13), 135303 (2009).

15. D.K. Bora, A. Braun, S. Erat, A.K. Ariffin, R. Löhnert, K. Sivula, J. Töpfer, M. Grätzel, R. Manzke, T. Graule, and E.C. Constable: Evolution of an oxygen near-edge X-ray absorption fine structure transition in the upper hubbard band in α-Fe$_2$O$_3$ upon electro-chemical oxidation. *J. Phys. Chem. C* **115**(13), 5619 (2011).

16. R.R. Rangaraju, K.S. Raja, A. Panday, and M. Misra: An investigation on room temperature synthesis of vertically oriented arrays of iron oxide nanotubes by anodization of iron. *Electro-chim. Acta* **55**(3), 785 (2010).

17. E.A. Garcla: Dynamical diffusion model to simulate the oxide crystallization and grain growth during oxidation of zirconium at 573 and 623 K. *J. Nucl. Mater.* **224**, 299 (1995).

18. X-w. Wei and C-y. Chen: Influence of oxidation heat on hard anodic film of aluminum alloy. *Trans. Nonferrous Met. Soc. China* **22**(11), 2707 (2012).

19. D. Graeve, H. Terryn, and G.E. Thompson: Influence of heat transfer on anodic oxidation of aluminium. *J. Appl. Electrochem.* **32**, 73 (2002).

20. A.M. Abd-Elnaiem, A.M. Mebed, A. Gaber, and M.A. Abdel-Rahim: Effect of the anodization parameters on the volume expansion of anodized aluminum films. *Int. J. Electrochem. Sci.* **8**, 10515 (2013).

21. A. Saijo, K. Murakami, M. Hino, and T. Kanadani: Effect of environmentally friendly anodization on the mechanical properties and microstructure of AZ91D magnesium alloy. *Mater. Trans.* **49**(5), 903 (2008).

22. S. Chatman, C.I. Pearce, and K.M. Rosso: Charge transport at Ti-doped hematite (001)/aqueous interfaces. *Chem. Mater.* **27**(5), 1665 (2015).

23. A. Yogi and D. Varshney: Cu doping effect of hematite (α-Fe$_{2-x}$Cu$_x$O$_3$): Effect on the structural and magnetic properties. *Mater. Sci. Semicond. Process.* **21**, 38 (2014).

24. Y. Hu, D.K. Bora, F. Boudoire, F. Häussler, M. Grätzel, E.C. Constable, and A. Braun: A dip coating process for large area silicon-doped high performance hematite photoanodes. *J. Renewable Sustainable Energy* **5**(4), 043109 (2013).

25. V.M. Aroutiounian, V.M. Arakelyan, G.E. Shahnazaryan, H.R. Hovhannisyan, H. Wang, and J.A. Turner: Photoelec-trochemistry of tin-doped iron oxide electrodes. *Solar Energy* **81**(11), 1369 (2007).

26. H-J. Ahn, M-J. Kwak, J-S. Lee, K-Y. Yoon, and J-H. Jang: Nanoporous hematite structures to overcome short diffusion lengths in water splitting. *J. Mater. Chem. A* **2**, 19999 (2014).

27. Z. Liu, K. Wang, L. Xiao, X. Chen, X. Ren, J. Lu, and L. Zhuang: A morphology effect of hematite photoanode for photoelectro-chemical water oxidation. *RSC Adv.* **4**, 37701 (2014).

28. R. Schrebler, L.A. Ballesteros, H. Gomez, P. Grez, R. Cordova, E. Munoz, R. Schrebler, J.R. Ramos-Barrado, and E.A. Dalchiele: Electrochemically grown self-organized hematite nanotube arrays for photoelectrochemical water splitting. *J. Electrochem. Soc.* **161**(14), H903 (2014).

29. H. Niu, S. Zhang, Q. Ma, S. Qin, L. Wan, J. Xu, and S. Miao: Dye-sensitized solar cells based on flower-shaped α-Fe$_2$O$_3$ as a photoanode and reduced graphene oxide–polyaniline composite as a counter electrode. *RSC Adv.* **3**(38), 17228 (2013).

30. K. Gajda-Schrantz, S. Tymen, F. Boudoire, R. Toth, D.K. Bora, W. Calvet, M. Gratzel, E.C. Constable, and A. Braun: Formation of an electron hole doped film in the alpha-Fe$_2$O$_3$ photoanode upon electrochemical oxidation. *Phys. Chem. Chem. Phys.* **15**(5), 1443 (2013).

31. A. Braun, Q. Chen, D. Flak, G. Fortunato, K. Gajda-Schrantz, M. Gratzel, T. Graule, J. Guo, T.W. Huang, Z. Liu, A.V. Popelo, K. Sivula, H. Wadati, P.P. Wyss, L. Zhang, and J. Zhu: Iron resonant photoemission spectroscopy on anodized hematite points to electron hole doping during anodization. *ChemPhysChem* **13**(12), 2937 (2012).

32. K. Maabong, A.G. Machatine, Y. Hu, A. Braun, F.J. Nambala, and M. Diale: Morphology, structural and optical properties of iron oxide thin film photoanodes in photoelectrochemical cell: Effect of electrochemical oxidation. *Phys. B* **480**, 91 (2016).

33. S. Heiroth, R. Frison, J.L.M. Rupp, T. Lippert, E.J. Barthazy Meier, E. Müller Gubler, M. Döbeli, K. Conder, A. Wokaun, and L.J. Gauckler: Crystallization and grain growth characteristics of yttria-stabilized zirconia thin films grown by pulsed laser de-position. *Solid State Ionics* **191**(1), 12 (2011).

34. V.D. Mote, Y. Purushotham, and B.N. Dole: Williamson-Hall analysis in estimation of lattice strain in nanometer-sized ZnO particles. *J. Theor. Appl. Phys.* **6**(6), 1 (2012).

35. Y. Caglar, S. Ilican, M. Caglar, F. Yakuphanoglu, J. Wu, K. Gao, P. Lu, and D. Xue: Influence of heat treatment on the nanocrystal-line structure of ZnO film deposited on p-Si. *J. Alloys Compd.* **481**(1–2), 885 (2009).

36. M.J. Jackson and W. Ahmed: Anodization: A promising nano-modification technique of titanium-based implants for ortho-pedic applications. In *Surface Engineered Surgical Tools and Medical Devices*, M. Jackson and W. Ahmed eds.; Springer: 2007; p. 21.

37. S-C. Shei, S-J. Chang, and P-Y. Lee: Rinsing effects on successive ionic layer adsorption and reaction method for deposition of ZnO thin films. *J. Electrochem. Soc.* **158**(3), H208 (2011).

38. R.M. Cornell and U. Schwertmann: *The Iron Oxides: Structure, Properties, Occurrences, and Uses* (Wiley-VCH, 2003).

39. F. Li, L. Zhang, and R.M. Metzger: On the growth of highly ordered pores in anodized aluminum oxide. *Chem. Mater.* **10**, 2470 (1998).

40. M.R. Belkhedkar and A.U. Ubale: Preparation and characteriza-tion of nanocrystalline α-Fe$_2$O$_3$ thin films grown by successive ionic layer adsorption and reaction method. *Int. J. Mater. Chem.* **5**(4), 109 (2014).

41. S.H. Tamboli, G. Rahman, and O-S. Joo: Influence of potential, deposition time and annealing temperature on photoelectrochem-ical properties of electrodeposited iron oxide thin films. *J. Alloys Compd.* **520**, 232 (2012).

42. V.M. Arutyunyan: Physical properties of the semiconductor-electrolyte interface. *Sov. Phys. Usp.* **32**(6), 521 (1989).